# 2-D primary beam shape measurements of the band-4, 550–850 MHz of the uGMRT

Santaji N. Katore and Dharam V. Lal
snk/dharam AT ncra DOT tifr DOT res DOT in

October 26, 2021

## Contents

## List of Figures



## List of Tables

**Abstract**

In interferometric images, knowledge of the primary beam is important in measurements of the flux densities and spectra of sources away from the pointing centre. Correction for the effect of the varying primary beam sensitivity is thus important in high dynamic imaging. Here, in this report, we present first measurements of the frequency dependent primary beam shapes for the band-4 ( 550–950 MHz) of the upgraded GMRT. These measurements would form a useful input for all users of the uGMRT.

# 1 Introduction

The recently accomplished upgrade of the GMRT (Gupta et al. 2017) has resulted in a significant increase in the instantaneous bandwidth of the telescope. This, it turn, leads to a significant increase in the sensitivity for continuum as well as pulsar studies. As part of the upgrade, all the antenna feeds, except the L-band feed have been replaced. Earlier measurements of the primary beam shape at Band-4 however were available only in the form of the best fit polynomial to an assumed azimuthally symmetric beam. Here we provide measurements of the actual 2-D shape of the beam in each polarization, which is significantly azimuthally asymmetric, as well as different for the two polarizations. However, for applications in which it is sufficient to assume an azimuthally symmetric polarization independent beam, we also provide polynomial fits to the same.

Note that the band-4 (550–850 MHz) feeds at the uGMRT are circularly polarized and they have been called as “RR”, “LL” and hence, the stokes I is labeled as “RRLL” at the GMRT. In this report, here we continue using this labeling. Here we use these basics (see also 2-D primary beam shape measurements of the band-5, 1050–1450 MHz of uGMRT, S.N. Katore & J.N. Chengalur, for more details) and present the methodology in Section 2, data analysis in Section 3, and summarize our findings in Section 5.

# 2 Methodology and data acquisition

The observations were made in the interferometric mode, using observations of 3C sources (3C286, 3C48 and 3C147). The default frequency setup for continuum band-4, 550–850 MHz band observations was used for all observations.

- Bandwidth = 200 MHz,
- No. of channel = 1024,
- Frequency Range = from 550 MHz to 750 MHz, and
- GAB LO = 550 MHz.

The antennas were scanned in the azimuth axis, with the multiple scans spaced $7'$ apart along the elevation axis. The scan rate was $40'$/minute and the integration time was either 2 second or 4 second. The grid size was selected to cover the beam at least up to the first null. For high dynamic range imaging applications one would need to determine the primary beam to still further distances than what our measurements provide. One would also need to know the full polar properties of the beam. As such, our measurements should be regarded only as a first step in the direction of characterizing the primary beam. We also note that the current feed positioning system at the GMRT has limited accuracy. This results in different primary beam shapes every time a feed is brought to focus. As such, it may in any case be difficult to apply the high dynamic range imaging techniques that use information about the primary beam. The current measurements may hence be adequate until the feed position system is upgraded.

# 3 Data analysis

After flagging out non functional antennas, the visibilities were used to determine antenna based gains, which was squared to get the power. The known raster scan rate and elevation position were used to convert the time-stamp of the data into the position on in the grid. The solution was computed independently for $\sim$0.39 MHz wide channels that are spaced $\sim$5 MHz apart to cover the frequency range from 550 MHz to 750 MHz. GNUPLOT was used to interpolate the observations onto a uniform grid in altitude and azimuth for each polarization. A 2-D elliptical Gaussian was fit to each data set using GNUPLOT to parametrize the beam shape. This parametrization is used to study the variation of the beam with frequency and polarization. Specifically the 2-D beam data grid was parametrized using a function of the form:

$$f(x, y) = A \times e^{-(a(x-x_0)^2 + 2b(x-x_0)(y-y_0) + c(y-y_0)^2)} \tag{1}$$

where,

$$a = \frac{cos^2\theta}{2\sigma_x^2} + \frac{sin^2\theta}{2\sigma_y^2},$$

$$b = \frac{sin2\theta}{4\sigma_x^2} + \frac{cos2\theta}{4\sigma_y^2},$$

and

$$c = \frac{sin^2\theta}{2\sigma_x^2} + \frac{cos^2\theta}{2\sigma_y^2}.$$

Here the coefficient $A$ is the amplitude, $x_0$, $y_0$ are the offsets from the center and $\sigma_x$, $\sigma_y$ are the $x$ and $y$ spreads of the beam (major and minor axis), from which the "half power beam width" (HPBW) or "full width at half maximum" can be computed. The angle $\theta$ indicates the position angle, in case of an elliptical beam. Where the HPBW are

$$\text{HPBW} = 2.35482 \times \sigma_x$$

and

$$\text{HPBW} = 2.35482 \times \sigma_y$$

for the major and minor axes, respectively. Furthermore, each Gaussian function is normalized to unity at the peak and the peak position was set to (0,0), i.e. the origin. Fig. 1 shows the Gaussian fits for the C 01 antenna at the centre frequency, 610 MHz of the band-4 (550–850 MHz) for the RR and LL polarizations.

The gridded data for all good antennas were averaged together (pixel by pixel) to increase signal to noise and a single average data set was formed. This was done separately for the RR and LL polarizations at each frequency channel. In addition a stokes I beam (labeled as "RRLL" in the Figures below) was generated by further averaging the data for the two polarization, RR and LL.

A total of six observing runs were performed spread over a period between 24 December 2017 and 19 February 2019. In addition to the average data sets as described above, an combined average (labeled as "AVG" in the Figures below) and a median (labeled as "MED" in the Figures below) were also computed over all the six observing runs.

# 4 Systematic trends in the measurements

Below we discuss beam ellipticity, dependence of beam-width on the frequency, polynomial fits for an azimuthally symmetric beam profile, and the accuracy of these polynomial fits in order to understand systematic trends, if any in band-4, 550–850 MHz band data of the uGMRT.

## 4.1 Beam ellipticity

Fig. 2 shows the plot of the HPBW measured from the median of the six observing runs as a function of frequency. The three different colored points indicates the RR (shown in red), LL (shown in green) and RRLL (shown in blue). Recall that the RRLL label indicates stokes I. The solid/filled circles are for the azimuth (AZ) axis while the empty circles are for the elevation (EL) axis. Missing points, if any in the Fig. 2 and subsequent Figures below are due to the removal of the RFI affected data.

As can be seen the RR and LL beams are elliptical, with the ellipticity being more pronounced at the lower frequencies. The major axis of the two ellipses are also misaligned, with one beam being wider along the elevation axis and the other beam being wider along the azimuth axis. On the other hand the stokes I ("RRLL") beam has close to equal widths along the elevation and azimuth axes.

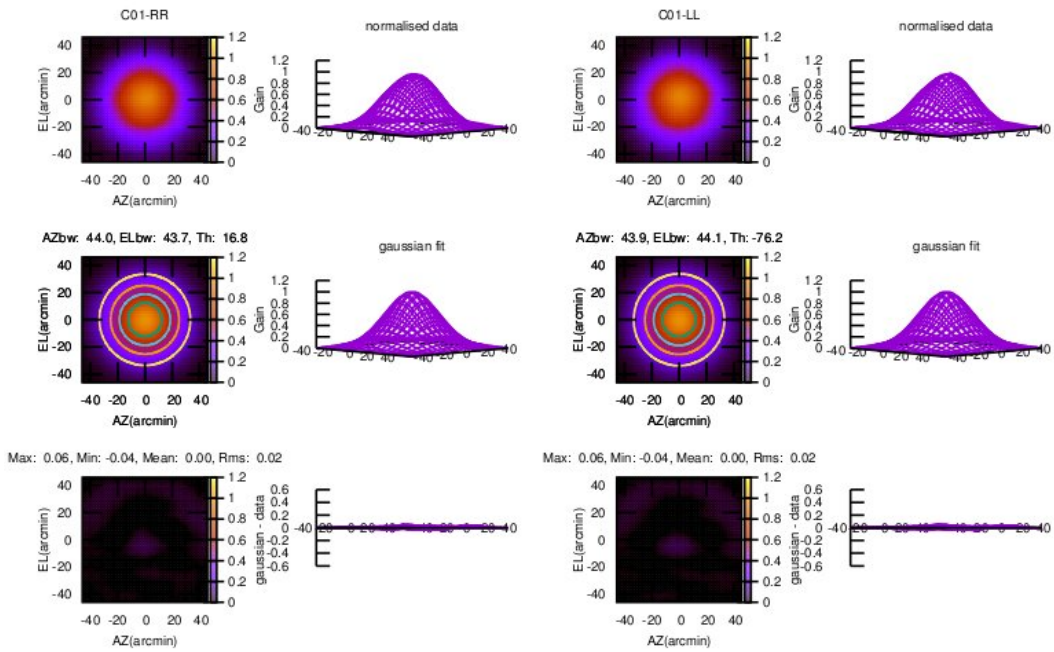


Figure 1: The data (top-panel) and the Gaussian fits (middle-panel) for the representative C 01 antenna at the centre frequency, 610 MHz of the band-4 (550–850 MHz) for the RR (left-column) and LL (right-column) polarizations. The bottom panel shows the difference between the data and the Gaussian fits showing the residuals.

## 4.2 Scaling with frequency

Naively one would expect the beam width to scale linearly with wavelength. However, since the feed illumination may vary in a non trivial manner with wavelength, deviations from this simple scaling are possible. We hence did fits of both first and second order polynomials to the HPBW as a function of frequency, *viz.*,

$$f(x) = \frac{\lambda}{a_1}$$

is the first order polynomial, and

$$f(x) = \frac{\lambda}{a_1} + \frac{\lambda^2}{a_2}$$

is the second order polynomial. Where $\lambda$ is wavelength, $a_1$ and $a_2$ are respectively the coefficients of the first and second order polynomials. The left-panel of Fig. 3 shows the first order polynomial fit to the beam width (RRLL) and the right panel shows the second order fit to the same beam width (RRLL). The fit to the data suggests that the second order polynomial fit is relatively better that the first order polynomial fit.

## 4.3 Azimuthally symmetric polynomial fits

As discussed above, the stokes I beam ("RRLL") can be reasonably well approximated to be azimuthally symmetric. For applications in which this approximation is sufficient we provide below 8th, 10th and 12th order polynomial fits to the beam.
The 8th order polynomial function is expressed as

$$f(x,y) = 1 + \frac{a}{10^3}(r\nu)^2 + \frac{b}{10^7}(r\nu)^4 + \frac{c}{10^{10}}(r\nu)^6 + \frac{d}{10^{13}}(r\nu)^8 \tag{2}$$

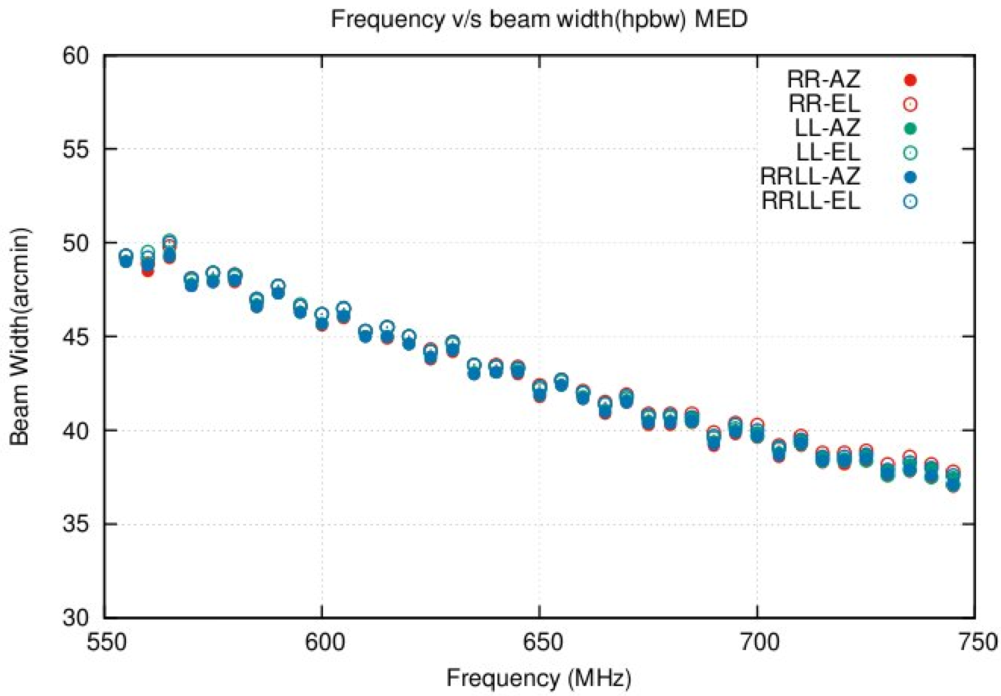


Figure 2: The plot showing the HPBW measured from the median of the six observing runs as a function of frequency. The three different colored points indicates the RR (shown in red), LL (shown in green) and RRLL (shown in blue). Recall that the RRLL label indicates stokes I. The solid-filled circles and empty circles are for the azimuth (AZ) and elevation (EL) axes, respectively. Missing points, if any, are due to the removal of RFI affected data.

The 10th order polynomial function is expressed as

$$f(x,y) = 1 + \frac{a}{10^3}(r\nu)^2 + \frac{b}{10^7}(r\nu)^4 + \frac{c}{10^{10}}(r\nu)^6 + \frac{d}{10^{13}}(r\nu)^8 + \frac{e}{10^{16}}(r\nu)^{10} \tag{3}$$

The 12th order polynomial function is expressed as

$$f(x,y) = 1 + \frac{a}{10^3}(r\nu)^2 + \frac{b}{10^7}(r\nu)^4 + \frac{c}{10^{10}}(r\nu)^6 + \frac{d}{10^{13}}(r\nu)^8 + \frac{e}{10^{16}}(r\nu)^{10} + + \frac{f}{10^{19}}(r\nu)^{12} \tag{4}$$

where,

$$r = \sqrt{x^2 + y^2}.$$

Here $r$ is the separation from the pointing position in arcmin, $\nu$ is the frequency in GHz, $a$, $b$, $c$, $d$, $e$ and $f$ are the coefficients of the polynomials. Figs. 4 and 5 show the median (MED) and the average (AVG) RRLL beams at the centre frequency 610 MHz of the 550-850 MHz data. These two Figures also show the corresponding model beam, the difference between the data and the model beams, and and this difference divided by the model beams. Note that in these two figures, we provide these model fits for 8th order polynomial, 10th order polynomial and 12th order polynomials fits for a faithful comparisons.

We also present the polynomial coefficients as a function of frequency for the three polynomials of 8th order (top-left panel), 10th order (top-right panel) and 12th order (bottom-left panel), respectively for the median (MED) RRLL beams in the three panels of Fig. 6. The coefficients themselves are also listed in Table 1.

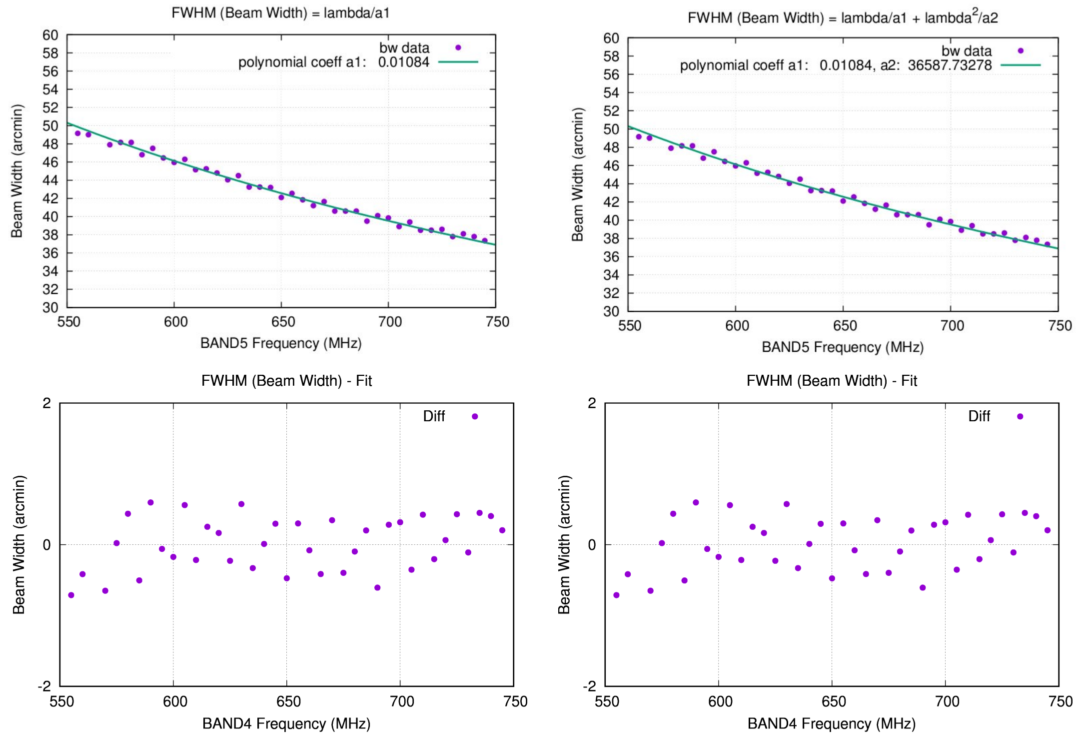


Figure 3: The upper left-panel shows the first order polynomial fit to the beam width (RRLL) data and the upper right-panel shows the second order polynomial fit to the same beam width (RRLL) data. The lower two panels shows the difference between the data and the model-fit for the first order polynomial fit (lower left-panel) and second order polynomial fit (lower right-panel).

### 4.4 Accuracy of the parametrization

In order to get an idea as to the expected accuracy of the primary beam correction, the RMS value of the difference between the median beam as well as the maximum ("MAX") value of the (absolute) difference was computed over both rings and annuli centered at the beam maximum. Fig. 7 show the rings and surface shapes used for this analysis. The sizes for the rings and annuli scale with the HPBW (for e.g. if HPBW = 44 arcmin, then 50% =22 arcmin, 100% = 44 arcmin, and 200% = 88 arcmin). The RMS and MAX values are computed for both the difference between the data and the polynomial models as well as the difference normalized by the model value at that location. The values for the 8th order polynomial, 10th order polynomial and 12th order polynomial fits are also plotted and tabulated (see Table 2) for different rings and surfaces and shapes. These plots (Figs. 9, 10 and 11) and table (Table 2) should provide users an indication of the expected error on the primary beam correction to the flux density. Note that for both, rings and surfaces shapes, the RMS' are $\lesssim$ 5% for 8th order polynomial, 10th order polynomial and 12th order polynomial fits. This suggests that higher order polynomial fits provide very little additional value, instead the 8th order polynomial is sufficient to provide meaningful science results.

The three panels, upper-panel, middle-panel, and lower-panels plots of Fig. 8 show the comparisons between the 8th order, 10th order and 12th order polynomial fits, the comparison between various surface unnormalized RMS values of the 12th order polynomial fit, and the comparison between various rings normalized RMS values of the 12th order polynomial fit, respectively. The RMS' are given in Table 2.

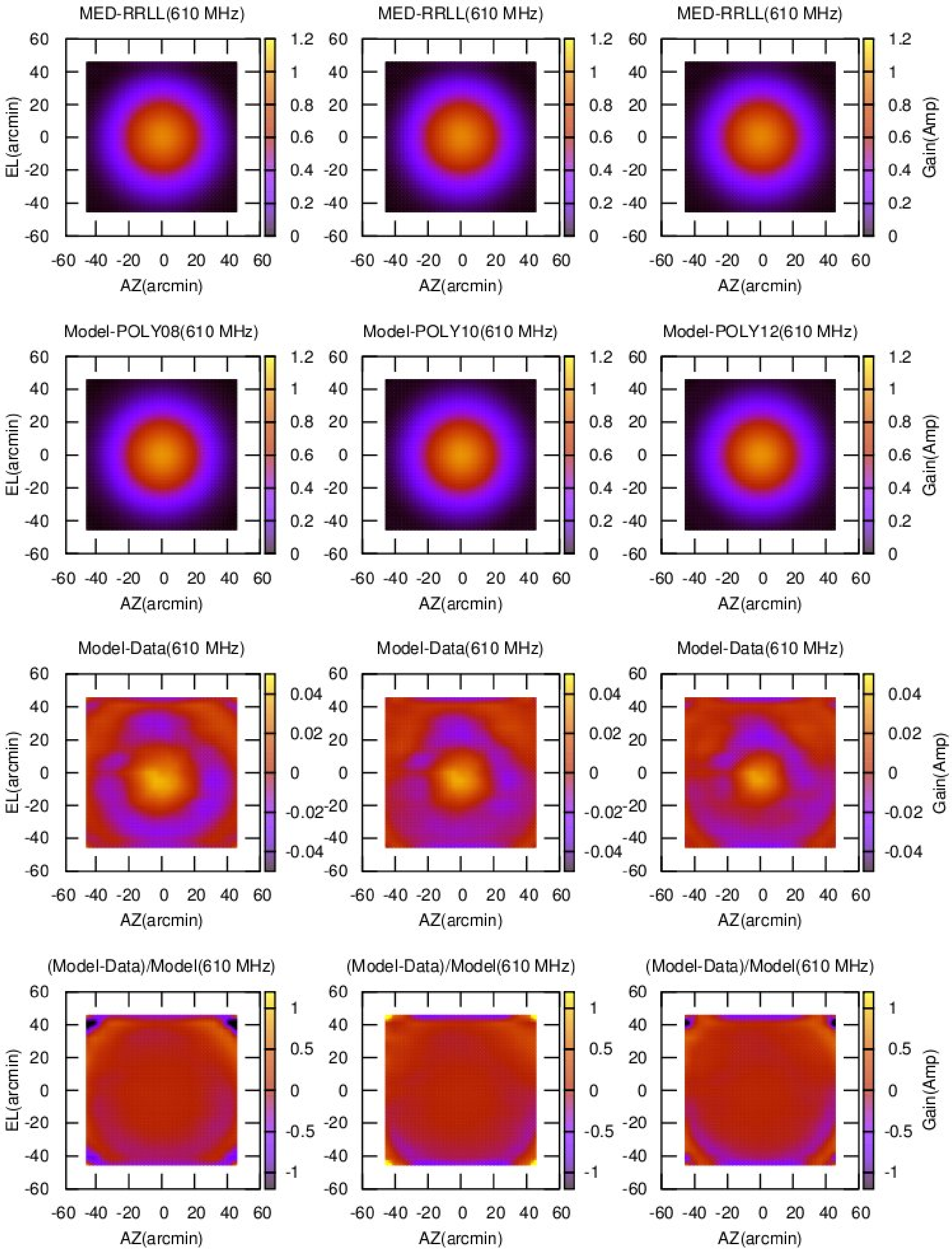


Figure 4: Figure showing the median (MED) RRLL beams at the centre frequency 610 MHz of the 550-850 MHz data. It also shows the corresponding model beams (second row panel), the difference between the data and the model beams (third row panel, and this difference divided by the model (fourth row panel). The three columns correspond to 8th order polynomial, 10th order polynomial and 12th order polynomial fits to the data.

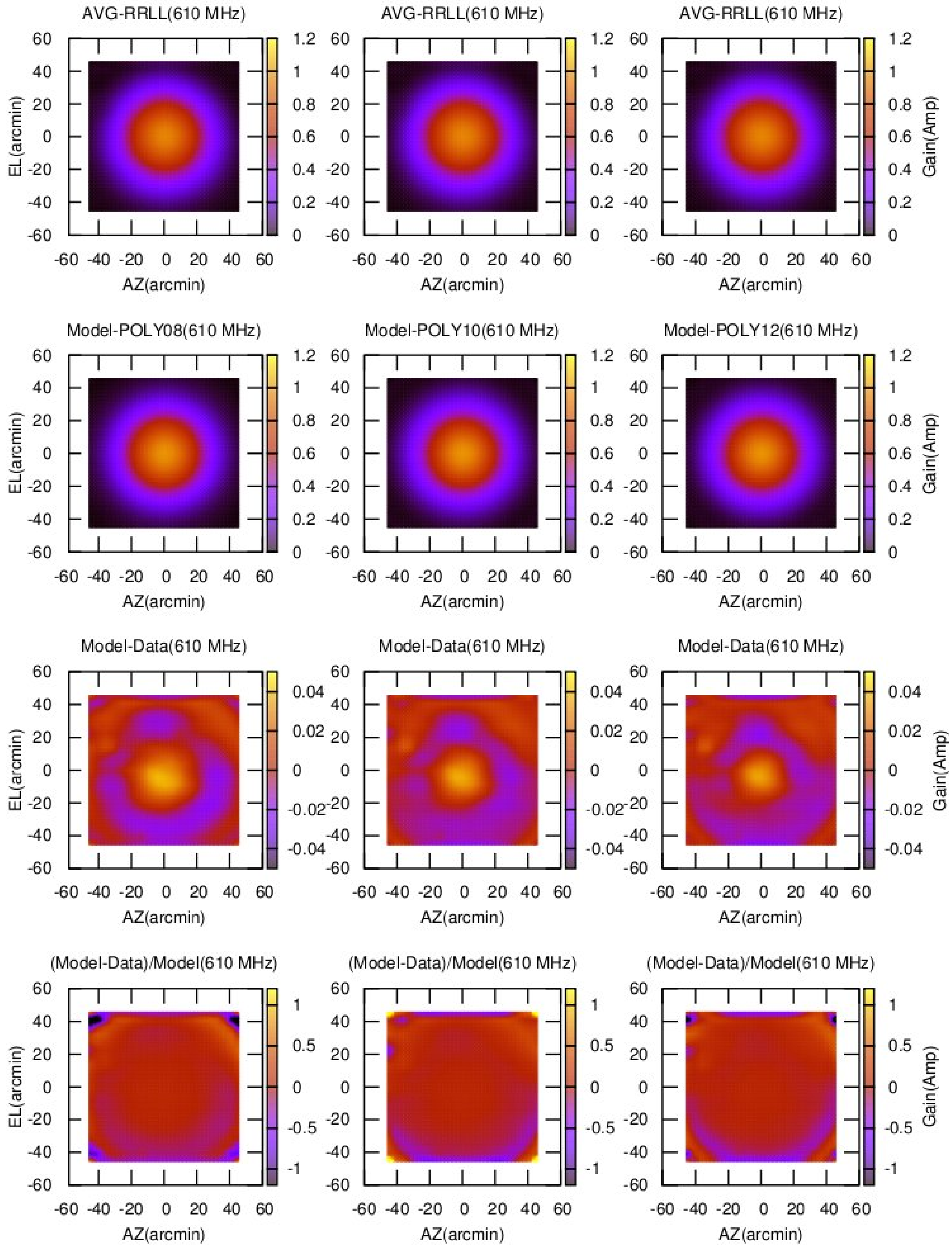


Figure 5: Figure showing the average (AVG) RRLL beams at the centre frequency 610 MHz of the 550-850 MHz data. It also shows the corresponding model beams (second row panel), the difference between the data and the model beams (third row panel, and this difference divided by the model (fourth row panel). The three columns correspond to 8th order polynomial, 10th order polynomial and 12th order polynomial fits to the data.

Table 1: The polynomial coefficients for the three polynomial fits of 8th order, 10th order and 12th order, respectively for the median (MED) RRLL beams. See also Sec. 4.3 and Fig. 6. Also detailed are the RMS', "data minus model" values for the 200% surface fit to should comparisons between these three polynomial fits.

| Order | Polynomial coefficients | | | | | |
|---|---|---|---|---|---|---|
| | $a$ | $b$ | $c$ | $d$ | $e$ | $f$ |
| 8th | −3.2625759 | 42.6183946 | −25.580447 | 5.82331466 | | |
| 10th | −3.4108297 | 51.9681333 | −44.463569 | 20.9821123 | −4.1919908 | |
| 12th | −3.5430929 | 63.8006369 | −80.122723 | 68.5616799 | −33.125335 | 6.53938614 |
| | RMS values, "data minus model" for the 200% (HPBW) surface fit. | | | | | |
| 8th | | 0.0133 | | | | |
| 10th | | 0.0121 | | | | |
| 12th | | 0.0112 | | | | |

Table 2: Table showing RMS', data minus model (HPBW) for both, the surface and ring shapes shown in Fig. 7 of the 8th order polynomial, 10th order polynomial and 12th order polynomial fits for the (MED) RRLL beams. See also Sec. 4.4 for a detailed discussion and Fig. 8 for comparisons between 8th order polynomial, 10th order polynomial and 12th order polynomial fits.

| RMS values, "data minus model" for 8th order, 10th order and 12th order polynomial fits | | | | | | | |
|---|---|---|---|---|---|---|---|
| Surfaces | RMS | | | Rings | RMS | | |
| | $8^{th}$ | $10^{th}$ | $12^{th}$ | | $8^{th}$ | $10^{th}$ | $12^{th}$ |
| 25% | 0.0326 | 0.0317 | 0.0310 | 0–25% | 0.0326 | 0.0317 | 0.0310 |
| 50% | 0.0288 | 0.0261 | 0.0242 | 25–50% | 0.0275 | 0.0241 | 0.0213 |
| 75% | 0.0233 | 0.0199 | 0.0180 | 50–75% | 0.0173 | 0.0119 | 0.0099 |
| 100% | 0.0187 | 0.0166 | 0.0158 | 75–100% | 0.0088 | 0.0084 | 0.0091 |
| 125% | 0.0163 | 0.0147 | 0.0136 | 100–125% | 0.0089 | 0.0095 | 0.0088 |
| 150% | 0.0150 | 0.0131 | 0.0118 | 125–150% | 0.0104 | 0.0080 | 0.0086 |
| 175% | 0.0136 | 0.0121 | 0.0115 | 150–175% | 0.0107 | 0.0098 | 0.0096 |
| 200% | 0.0133 | 0.0121 | 0.0112 | 175–200% | 0.0106 | 0.0101 | 0.0103 |

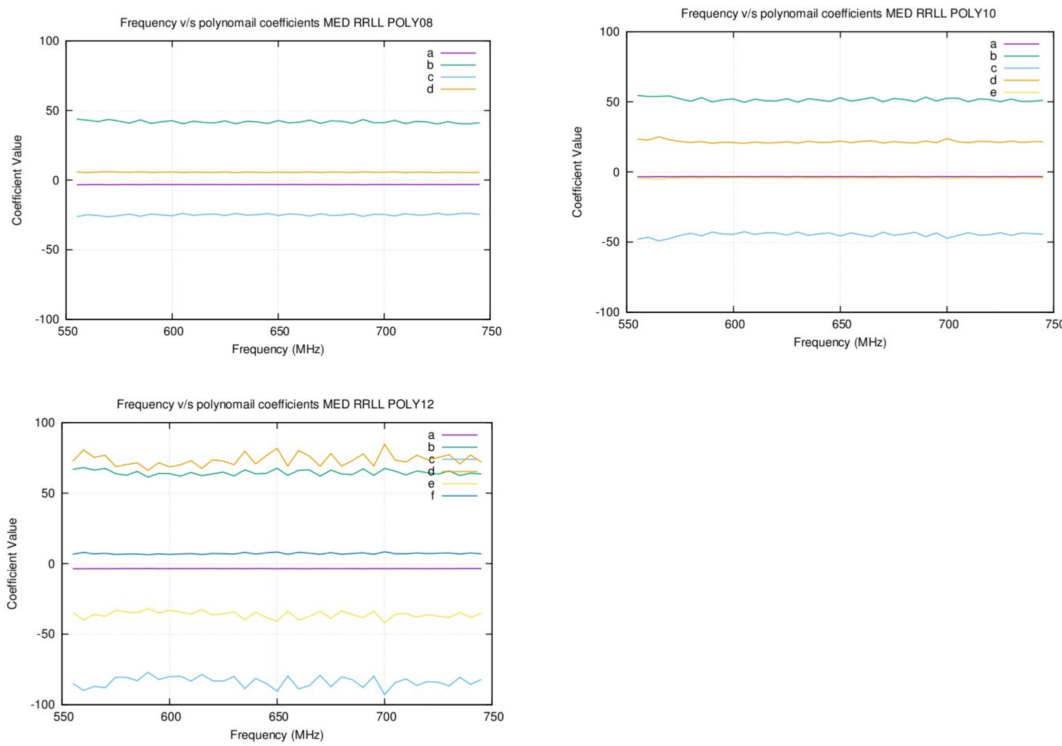


Figure 6: Figure showing polynomial coefficients as a function of frequency for the three polynomials of 8th order (top-left panel), 10th order (top-right panel) and 12th order (bottom-left panel) respectively. The coefficients themselves are also listed in Table 1.

# 5 Summary of Results

We hope that this document, in particular Table 1 would be useful for the users of the GMRT in order to perform appropriate system checks, thereby improve the performance of the GMRT images at band-4 (550–850 MHz).

In Figs. 4 and 5, we provide comparisons of the median and average RRLL beams at the centre frequency 610 MHz of the 550-850 MHz data. They also present the corresponding model beams, the difference between the data and the model beams, and this difference divided by the model for the 8th order polynomial, 10th order polynomial and 12th order polynomial fits to the data.

- Clearly there are no appreciable differences that are shown in the 10th order polynomial or the 12th order polynomial fits as compared to the 8th order polynomial fit.
- Furthermore, the accuracy of parametrization using the surfaces and rings (as detailed in Sec. 4.4) too do not reveal appreciable differences between the 10th order polynomial or the 12th order polynomial fits as compared to the 8th order polynomial fit (see also Table 1.

Although we provide a variety of Figures for users of the uGMRT to make a judgement re. the nature of polynomial fits, we believe that the 8th order polynomial is sufficient to draft science conclusions for the band-4, 550-850 MHz band of the uGMRT.

# 6 References


- Gupta, Y., et al. 2017 Cu. Sci. 113, 707
- Katore, S. N. & Chengaulr, J. N. 2-D primary beam shape measurements of the band-5, 1050–1450 MHz of the uGMRT

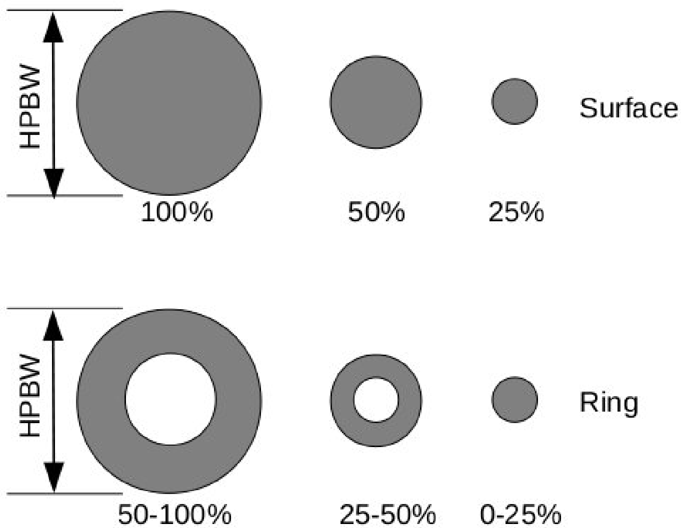


Figure 7: Figure showing the rings and surface shapes used to understand the expected accuracy of the primary beam correction. The sizes for the rings and annuli scale with the HPBW (for e.g., if HPBW = 44 arcmin, then 50% =22 arcmin, 100% = 44 arcmin, and 200% = 88 arcmin). See also Table 2 showing RMS' for both, the surface and ring shapes of the 8th order polynomial, 10th order polynomial and 12th order polynomial fits.

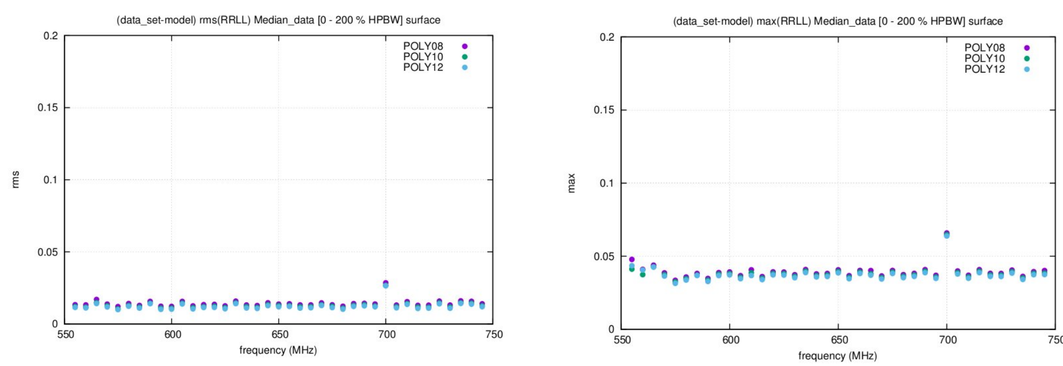


Figure 8: Plots showing the comparisons between the 8th order, 10th order and 12th order polynomial fits.

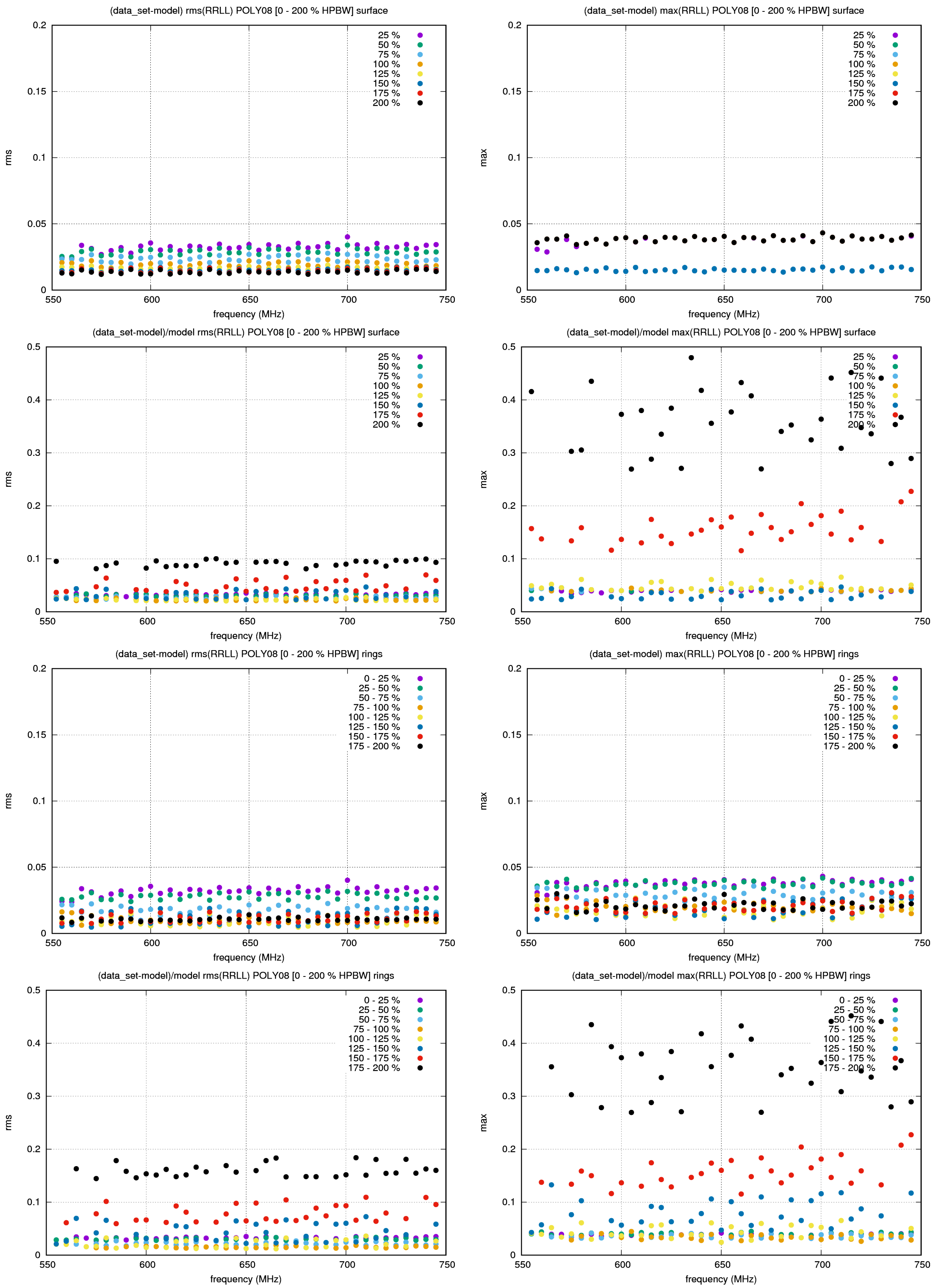


Figure 9: Plots showing the comparison between various surfaces and rings for the RMS values (left column panels) and the MAX values (right column panels) of the 8th order polynomial fits. The first and third row panels show the unnormalised (data minus model) polynomial fits and the third and fourth row panels show the normalised (data minus model divided by the model) polynomial fits.

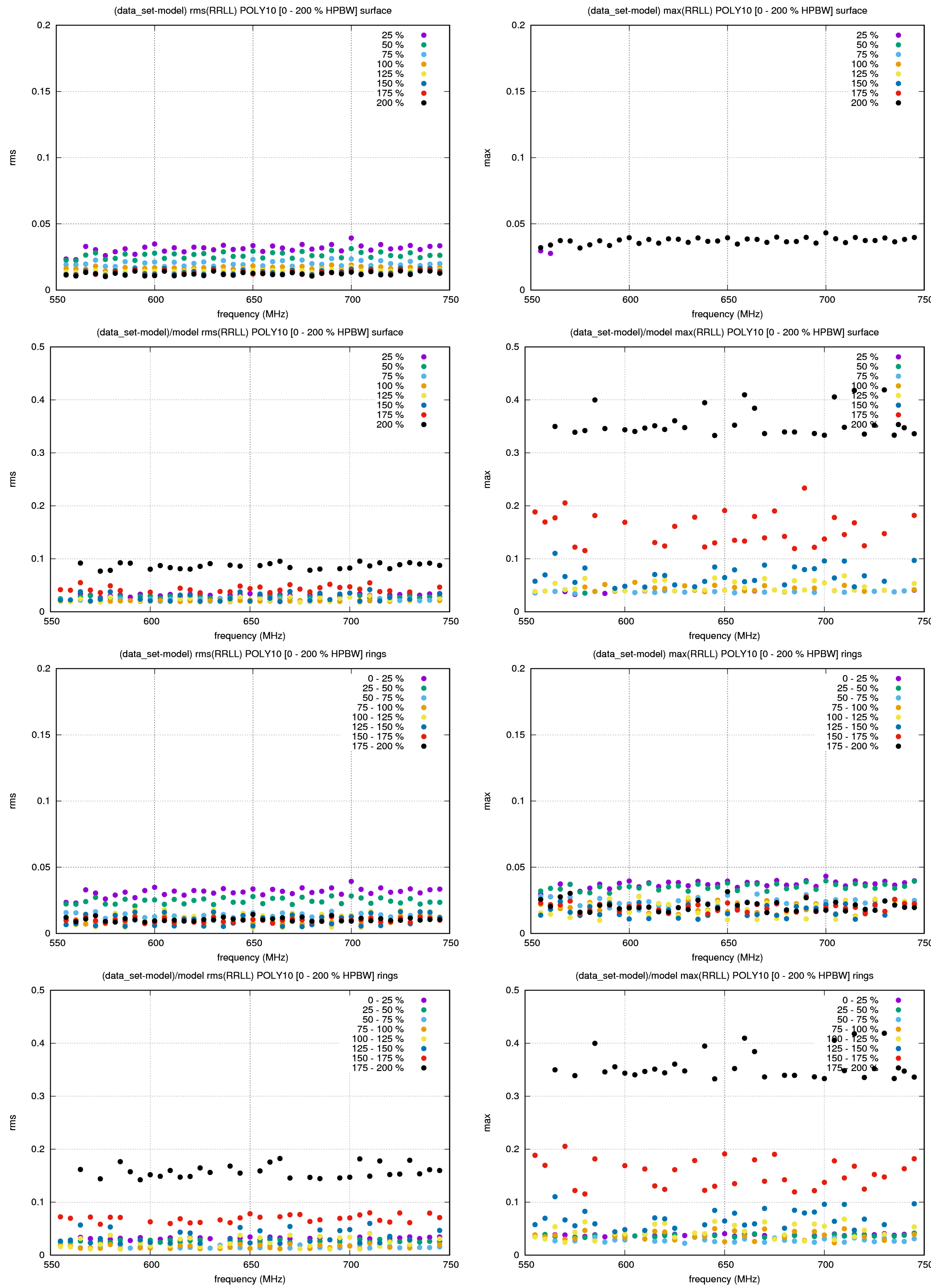


Figure 10: Plots showing the comparison between various surfaces and rings for the RMS values (left column panels) and the MAX values (right column panels) of the 10th order polynomial fits. The first and third row panels show the unnormalised (data minus model) polynomial fits and the third and fourth row panels show the normalised (data minus model divided by the model) polynomial fits.

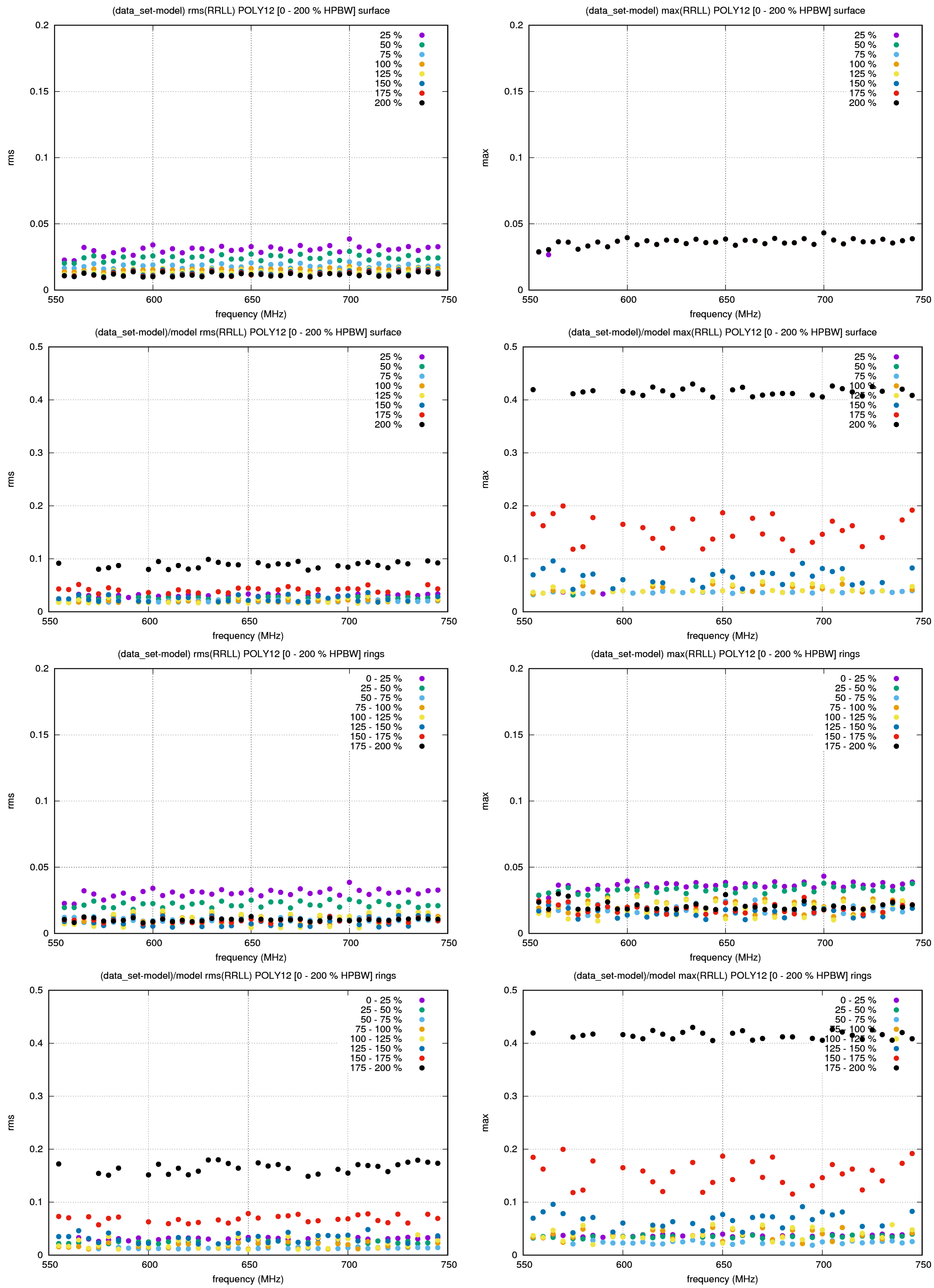


Figure 11: Plots showing the comparison between various surfaces and rings for the RMS values (left column panels) and the MAX values (right column panels) of the 12th order polynomial fits. The first and third row panels show the unnormalised (data minus model) polynomial fits and the third and fourth row panels show the normalised (data minus model divided by the model) polynomial fits.